# Numerical Study of Cold Gas Micronozzle Flows

M.S. Ivanov[†]and G.N. Markelov[*]
*Institute of Theoretical and Applied Mechanics,*
*Novosibirsk 630090, Russia*

A.D. Ketsdever[‡]
*Air Force Research Laboratory*
*Propulsion Directorate*
*Edwards AFB, California*

D.C. Wadsworth[§]
*Raytheon STX*
*Edwards AFB, California*

**20010226 052**

## 1. Introduction

Due to their simplicity, low-thrust cold-gas propulsion systems have the potential to provide orbital maneuvering capability for small, micro- and even nano-satellites.

Each specific mission where cold gas thrusters will be used places a unique set of requirements on the system. For example, micro-spacecraft with masses of $1 - 50$ kg, will require thrust levels for typical orbital maintenance maneuvers of $0.1 - 10$mN. Missions which require precise attitude control, where the most important factor is a very low thrust, will require thrust levels between $10 - 100\mu$N.

To obtain these low thrust values, small nozzle dimensions and low chamber pressures are usually used. These result in the throat Reynolds number, $Re_t = 2\dot{m}/\pi\mu_0 R_t$, on the order of 10 to $10^3$. Here, the quantity $\dot{m}$ is the mass flow rate, $R_t$ is the throat radius, and $\mu_0$ is the propellant gas viscosity at the stagnation chamber temperature. Due to the low Reynolds number, viscous losses are significant in small scale nozzles.

The availability of micromachined cold gas thrusters creates new possibilities for creating effective low thrust propulsion systems. This is due to

---

† Head, Computational Aerodynamics Lab. Senior Member, AIAA. E-mail ivanov@itam.nsc.ru
* Research Scientist, Computational Aerodynamics Lab.
‡ Senior Research Engineer, Senior Member, AIAA.
§ Principle Scientist

a possibility of manufacturing nozzles with a throat size of $10\mu$m and which use high chamber pressures (1-10 atm). This permits low thrust levels for rather high Reynolds numbers. For instance, for axisymmetric nozzles with a fixed area ratio, a ten-fold change in the linear dimension requires a 100-fold increase in the chamber pressure to preserve a prescribed thrust level. However, the throat Reynolds number increases only by a factor of ten, and the problem of taking into account viscous losses remains.

To model these types of gas flows, Navier–Stokes (NS) and Direct Simulation Monte Carlo (DSMC) techniques are commonly used. The weaknesses of the NS approach as applied to rarefied flows are well known in a qualitative sense. At sufficiently low $Re_t$, reliable results can be obtained only on the basis of kinetic approach, for example, by the DSMC method[1]. The computational cost of the DSMC method, however, rapidly increases as the Reynolds number increases.

A performance evaluation for a 2D micronozzle was performed using the NS equations in Ref.[2] for Reynolds numbers $Re_t = 500 - 10000$ and by the DSMC[3] method for $Re_t = 1 - 160$. The authors[4] used a combined Navier–Stokes/DSMC approach to analyze nozzle flows at low Reynolds numbers. To decrease the computational cost, the DSMC calculation was performed only for the supersonic section of the nozzle. The development of numerical algorithms of the DSMC method as well as an increase of computer power allows the calculation of the entire nozzle for Reynolds numbers of 500 and higher[5], which is close to the area of applicability of the Navier–Stokes equations.

The objective of the present paper is to compare local flowfield and integrated performance properties of low-density nozzles exhausting into a perfect vacuum as predicted by the continuum method

1

based a finite volume approximation of NS equations, and the DSMC method based on molecular gasdynamics. The calculations were performed for a conical micronozzle in the range of Reynolds numbers $Re_t = 130 - 1300$ and for the Rothe[6] nozzle for $Re_t = 120$ and 270 (corresponding to Rothe's $B = 260$ and 590). These comparisons are expected to provide design guidance for nozzles which may experience low Reynolds number flow due to low stagnation pressure or due to small characteristic throat dimension (micronozzles). For both of these types of nozzles, viscous and rarefaction effects can lead to severe performance degradation relative to ideal nozzle predictions. Since the NS approach is typically much more computationally efficient, it may be preferable to DSMC for many design tasks if sufficient confidence in its ability to predict the performance of this class of nozzles can be established.

Several authors have previously simulated the Rothe nozzle using both simplified[7] and more complete[8] forms of the NS equations and also DSMC,[9] however, these focused for the most part on comparison with local measurements made on the centerline of the nozzle diverging section rather than integrated performance quantities more directly useful to nozzle design studies. It will be shown that the NS results agree rather well with the centerline data even at relatively low operating pressure or $Re_t$, however, the trends in specific impulse (or thrust) begin to appear non-physical at these same pressures. For the micronozzle, no experimental data are available, and only comparisons between the DSMC and NS results are made as a function of operating pressure and nozzle geometry. The lowest pressure considered leads to non-physical behavior of the NS-predicted thrust. Detailed comparison of the predicted flowfields between the methods facilitates understanding of the deficiencies in the NS approach.

## 2. Nozzle Geometry

### 2.1. Micronozzle

A conical micronozzle with a 54.7° or 30° angle converging section and 15° angle diverging section (Fig. 1) used for the computations. The nozzle can be routinely fabricated by etching silicon. The nozzle has a sharp corner at the throat, an exit diameter of 81.3 $\mu$m, and develops a thrust of 1 mN for 10 atm chamber pressure of helium. Chamber and wall temperatures were $T_0 = T_w = 297$ K. Chamber pressure was changed from 10 to 1 atm for a performance evaluation, which corresponded to a change in the throat Reynolds number from 1300 to 130.
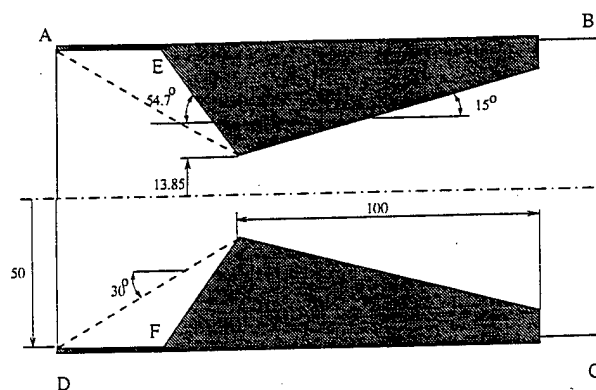


Fig. 1 Geometry of micronozzle

### 2.2. Rothe nozzle

Calculations were also made to directly compare with the experimental data of Rothe.[6] The subsonic and supersonic portions of the nozzle are cones having half-angles 30° and 20°, respectively, with longitudinal radii of curvature at the throat equal to one-half of the throat radius. The test gas was nitrogen at $T_0 = 300$ K. The throat Reynolds numbers were $Re_t = 270$ and 120.

## 3. Numerical approaches

### 3.1. Continuum approach

Continuum solutions are generated with the full Navier–Stokes code GASP[10]. The nominal grid contains 257 axial and 129 radial points, with clustering in both directions to resolve gradients across the throat and in the wall boundary layer. The inlet is modeled as a subsonic Riemann inflow boundary with an assumed stagnation number density and temperature, and Mach number based on the ideal one-dimensional nozzle value at the inlet area ratio. Fixed stagnation pressure and temperature boundary conditions were also attempted, but were abandoned due to code instabilities. First order extrapolation is used at the outflow boundary. These boundary conditions are usually used for nozzle flow modeling. It is assumed that the use of extrapolation for subsonic portion of the boundary layer at the nozzle exit does not affect nozzle performance[8]. For the Rothe nozzle cases, calculations were made for both adiabatic and constant temperature ($T_w = T_0$) and no-slip wall boundary conditions. The experimental results suggest that the wall is adiabatic, however, the constant wall temperature calculations

were made to evaluate the effect of the wall boundary conditions on the flow structure and integrated performance properties. For the micronozzle, a no-slip, constant temperature ($T_w$=297 K) wall was assumed.

Results were post-processed to extract integrated performance, local flowfield, and wall properties. The axial mass flow and inviscid momentum flux (thrust) were interpolated onto each axial cell-face and summed at each axial station to monitor solution quality and also provide a local measure of nozzle performance. The nominal grid shows a maximum axial variation of mass flow of below one percent (Fig. 2). Oscillations in total mass flow are noticeable at the throat, due presumably to the interpolation procedure, and at each boundary, due to interpolation and also potentially the boundary condition treatment. Momentum flux oscillations are much smaller. The specific impulse profiles show negligible oscillation. Grid sequencing studies confirm that the integrated profiles are essentially independent of grid size for a grid of 129x32 points or larger (Table. 1).
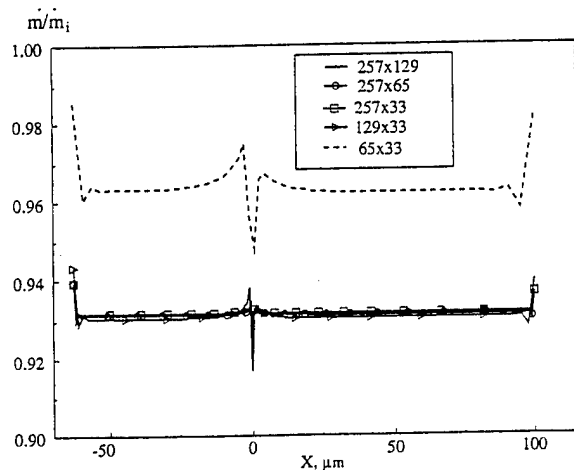
Fig. 2 Variation of axial mass flow for different nominal grids (micronozzle at 10 atm chamber pressure)

### 3.2. Kinetic approach

The DSMC code SMILE was used in the present work, which was effectively used previously for jet flows[11] and nozzle flows[5]. The following features of the code are important for computations were performed:

1). *The method that combines majorant cell and free cell schemes*[12] of the DSMC. The computational domain is divided into uniform so-called background

| grid size | $\dot{m}/\dot{m}_i$ | thrust, mN | $I_{sp}/I_{sp_{ideal}}$ |
|---|---|---|---|
| 257x129 | 0.9313 | 0.8746 | 0.9840 |
| 257x65 | 0.9313 | 0.8747 | 0.9840 |
| 257x33 | 0.9316 | 0.8752 | 0.9840 |
| 129x33 | 0.9304 | 0.8727 | 0.9840 |
| 65x33 | 0.9631 | 0.8992 | 09835 |

Table 1 The influence of grid size on the integrated parameters (micronozzle at 10 atm chamber pressure)

cells. Each background cell has its own interaction parameter. This parameter governs the local collision resolution. The adaptation of the resolution to local gradients and local mean free paths occurs during the modeling process. Such a combined usage of cell and free cell schemes made it possible to achieve adequate spatial resolution in the entire flow field (see Ref. [13]). In conjunction with the correct collision number for even small number of particles in a cell, this allows one to simulate the flow at very small Knudsen numbers.

2) *Adaptive grids.* Two different grids are utilized in the code: first one is for collision procedure, and second is for gas dynamic parameters sampling. The utilization of two different grids for collisions and macroparameters is rather important since different adaptation algorithms are in use for these grids. Adaptation of collision grids aims at an accordance of cell size to the value of local mean free path. The macroparameter grid catches generally the flow gradients and requires normally the number of cells much less than for collisions.

3). *Spatial weighting factors.* The most severe practical problem associated with DSMC calculations for axisymmetric flows is a small fraction of the molecules that are located near the axis. This has led to the introduction of *radial weighting factors* such that a molecule located far from the axis represents more real molecules than one near the axis.

4). *Adaptive decomposition onto subdomains with different time steps.* The strong differences in the number densities and flow gradients which are observed near to the throat, and those observed in the near vicinity of nozzle exit plane, make us split the computational domain into subdomains with different time steps ($\Delta t$). This splitting is performed in the course of computation and permits to compute the nozzle flow faster. An approach $F_{num}/\Delta t = const$ is used for coupling of these subdomains.

5). *Particle doubling.* One of the main reasons of

large computational cost is the long time required to establish the steady flow. The cost of unsteady stage exceeds often fifty percent of the whole computation. To overcome this problem, a special procedure of doubling of particles is used. Using the doubling procedure allows one to compute the unsteady stage rather fast at the successive increasing of the number of particles.

The diffuse law with complete accommodation was used for gas/surface interaction, and the VHS model[1] for intermolecular collisions. The Larsen–Borgnakke model[14] with temperature-dependent rotational collison number was used for a energy exchange between translational and rotational molecular modes. A total number of model particles in the computations was $1 \cdot 10^6 - 3 \cdot 10^6$ (depending on the value of the throat Reynolds number) in the entire computational domain ABCD (Fig. 1).

Two types of inlet radial velocity profiles (uniform and Poiseuille profiles) were considered in the present DSMC calculations. For the nozzle with a $54.7°$ convergence section the inlet plane was located at the entrance of convergence section (lines EF in Fig. 1) or at the entrance of cylindrical chanel (line AD). For the nozzle with a $30°$ convergence section, line AD, which is the beginning of convergence section, was also used as an inlet plane. The particles enter the flow domain in accordance to Maxwellian distribution function with density, temperature, and velocity obtained from isentropic relations. The mean velocity for Poiseuille profile equaled the uniform flow velocity.

As an example, Figure 3 shows the profiles of axial velocity near the nozzle throat for different inlet plane conditions listed in Table 2. It is seen that for all cases considered the mass flow rate and the vacuum specific impulse coincide. It should be noted that the formulation of stable and physically realistic inflow conditions at a subsonic boundary for both NS and DSMC techniques is a current research problem.

## 4. Results and Discussion

### 4.1. Micronozzle

Calculations of micronozzle flows are made for the different chamber pressures. Figure 4 shows Mach number contours obtained by two methods for $p_0 = 10$ atm. It is seen that the results are in good agreement in the throat area up to $x = 25\mu m$ ($M = 2.75$). Further downstream the difference increases. The inflections in the pressure contours indicate a weak compression wave forms near the
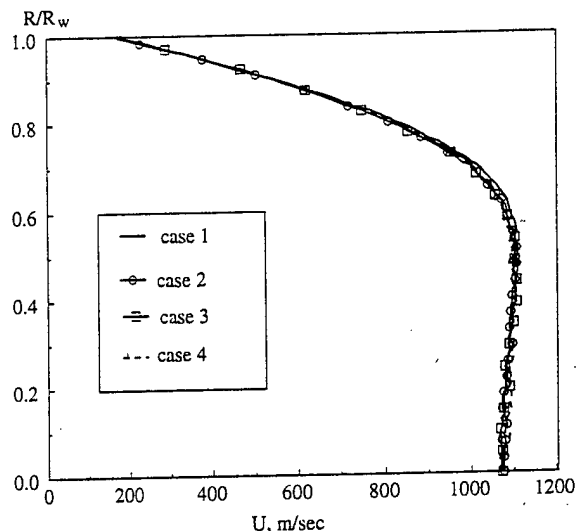
Fig. 3 Axial velocity profiles for different inlet conditions (micronozzle at 1 atm chamber pressure, x = $10\mu m$)

throat and is reflected at the nozzle symmetry line (Fig. 5). In solving the Navier–Stokes equations, the outflow boundary of the computational domain coincided with the nozzle exit plane, and the parameters at the nozzle exit plane were determined by extrapolation from inside. These boundary conditions result in the isoline $M = 1$ being propagated directly to the exit plane. In the kinetic model, a strong pressure gradient induced by gas exhaust into vacuum leads to flow acceleration near the nozzle lip, and the isoline $M = 1$ is terminated on the nozzle lip. The difference in the boundary conditions leads to a decrease of the subsonic section of the boundary layer in DSMC simulations and to a decrease of the incident angle of the compression wave. Obviously, not only the thickness of the subsonic section of the boundary layer decreases, but also the thickness of the boundary layer itself, which leads to a greater expansion of the flow: a greater Mach number and a lower pressure (Fig. 5). Thus, even for a rather small thickness of the subsonic section of the boundary layer the use of extrapolation leads to a significant difference between the continuum and kinetic results. These local features are known to greatly influence the near-exit plume or contamination backflow properties of the nozzle.

An additional factor that affects the flow structure is a rather large value of the slip velocity ($\sim 400$ m/sec at the nozzle lip). As long as the slip velocity does not exceed 100 m/sec, the pressures on the wall of the supersonic section of the nozzle are in fairly good agreement (Fig. 6). As the slip velocity

4

| case | 1 | 2 | 3 | 4 |
|---|---|---|---|---|
| angle of convergence section | 54.7 | 54.7 | 54.7 | 30 |
| location of inlet plane | line EF | line AD | line AD | line AD |
| velocity profile at inlet | Poiseuille | Poiseuille | uniform | uniform |
| $\dot{m}, kg/sec$ | 4.8421e-8 | 4.8676e-8 | 4.8394e-8 | 4.8388e-8 |
| thrust, mN | 0.073704 | 0.074517 | 0.074145 | 0.074283 |
| $I_{sp}, sec$ | 155.22 | 156.11 | 156.23 | 156.54 |

Table 2   The influence of inlet conditions on the micronozzle performance (1 atm chamber pressure)
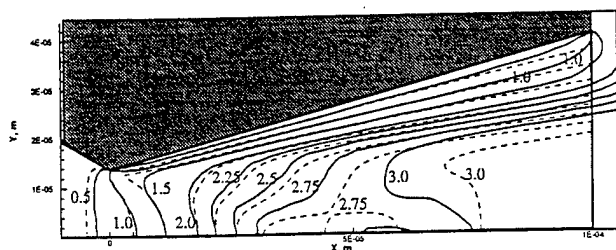


Fig. 4   Mach number contours (dashed lines - GASP, solid - SMILE, 10 atm chamber pressure)
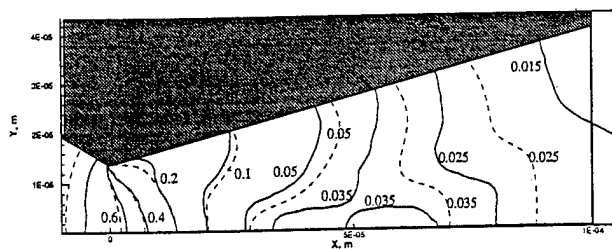


Fig. 5   Pressure isolines (dashed lines - GASP, solid - SMILE, 10 atm chamber pressure)



Fig. 6   Pressure distribution and slip velocity along the nozzle wall (chamber pressure is 10 atm)

increases downstream, the pressures differ by a factor of two. Obviously, the effect of the velocity slip is significant only inside the boundary layer. This is clearly shown in Fig. 7, which shows the profiles of the axial and radial velocities at the nozzle exit plane. In the core flow ($R/R_e \leq 0.6$) both numerical approaches give roughly equal velocities, but a substantial difference is observed inside the boundary layer.

Two criteria are usually used to evaluate the area of applicability of the continuum approach: breakdown parameter $B = M\sqrt{\frac{\pi\gamma}{8}}\frac{\lambda}{\rho}\left|\frac{d\rho}{ds}\right|$ and local Knudsen number $Kn = \frac{\lambda}{\rho}\left|\frac{d\rho}{ds}\right|$. $M$ is the Mach number, $\rho$ is the density, $\lambda$ is the local mean free path, and $s$ is the distance along the streamline. For the case

under consideration ($p_0 = 10$ atm), the breakdown parameter and local Knudsen number contours are shown in Figs. 8 and 9. It is seen that the critical value $B = 0.05$, which gives the border of the area of applicability of continuum approach, is reached only near the nozzle lip. It can be concluded, therefore, that the differences observed in the fields of gasdynamic parameters obtained using different approaches are explained only by the presence of slip at the wall and incorrect outflow boundary conditions used in solving the Navier–Stokes equations.

The situation becomes even worse when these boundary conditions are used for a lower chamber pressure ($p_0 = 1$ atm). In this case, the subsonic section of the boundary layer obtained using the Navier–Stokes equations is more than 30% of the exit radius, which makes a two-fold difference with the DSMC result (Fig. 10). This leads to the fact that the Mach number in the nozzle exit does not exceed $M = 1.8$, whereas the kinetic approach yields significantly higher Mach numbers up to $M = 2.7$.

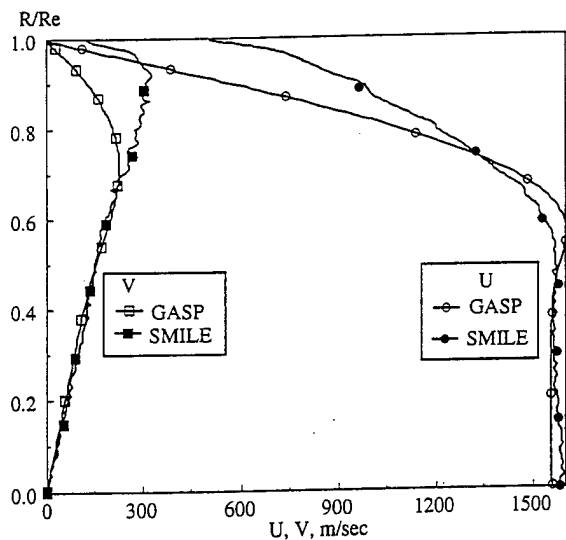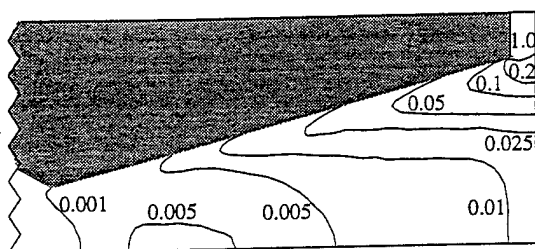Fig. 7 Axial U and radial V velocity profiles at nozzle exit plane



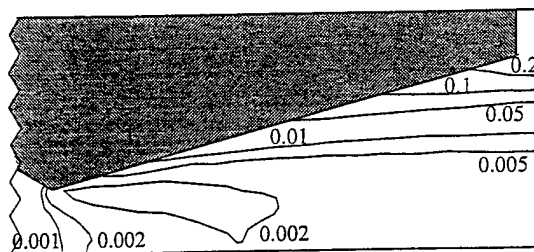Fig. 8 Breakdown parameter (10 atm chamber pressure, SMILE)



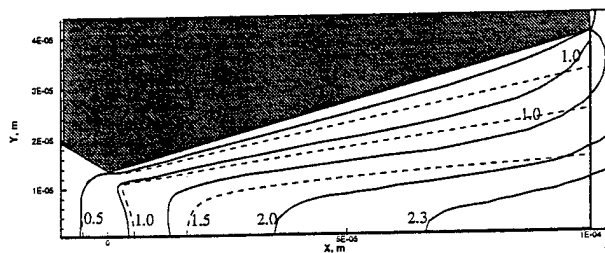Fig. 9 Local Knudsen numbers (10 atm chamber pressure, SMILE)



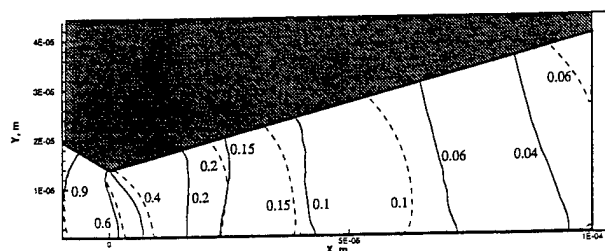Fig. 10 Mach number contours (dashed lines - GASP, solid - SMILE, 1 atm chamber pressure)



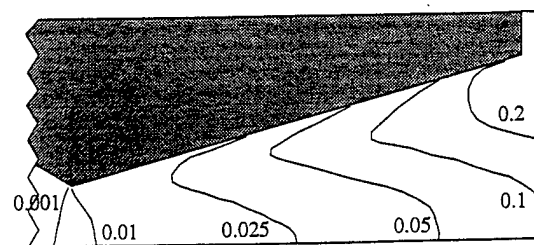Fig. 11 Pressure isolines (dashed lines - GASP, solid - SMILE, 1 atm chamber pressure)



Fig. 12 Breakdown parameter (SMILE, 1 atm chamber pressure)

For this micronozzle, the pressure fields obtained by the two approaches differ rather significantly, except in the vicinity of the throat (Fig. 11). Obviously, the continuum approach cannot be used for such a low pressure. The breakdown parameter reaches the critical value $B = 0.05$ approximately in the middle of the nozzle (Fig. 12). Figure 13 shows the nonequilibrium that arises between translational temperatures based on the thermal component of motion in the axial and radial directions. It is seen that the difference is observed not only near the nozzle lip, but also along the wall of the divergence section of the nozzle.
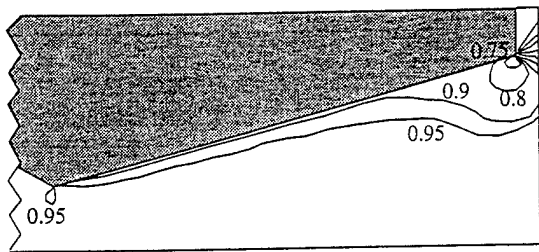
Fig. 13 Nonequilibrium of temperature $T_x/T_y$ (SMILE, 1 atm chamber pressure)

Velocity profiles presented in Fig. 14 show that the boundary layers practically fill the entire nozzle exit, and the presence of a significant slip velocity (up to 1000 m/sec) leads to a substantial radial spreading of the flow. The effect of a high pressure gradient at the nozzle exit plane extends upstream to the throat (Fig. 15). This demonstrates once again that the outflow boundary conditions used in the Navier–Stokes solution are invalid. Additional Navier–Stokes calculations are planned to address any influence that inclusion of the geometry and flowfield downstream of the nozzle exit plane has on these quantities.
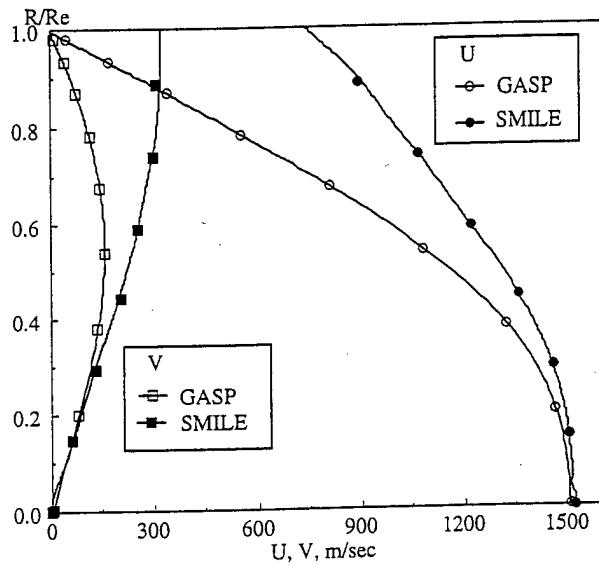


Fig. 14 Axial U and radial V velocity profiles at nozzle exit plane (1 atm chamber pressure)



Fig. 15 Pressure distribution and slip velocity along nozzle wall (chamber pressure is 1 atm))



Fig. 16 Density distribution along nozzle axis

Note that the use of the density distribution along the nozzle axis as a criterion of applicability of the continuum approach is not enough. The density distributions along the nozzle axis for the examined values of chamber pressure ($p_0 = 10$ and 1 atm), which were obtained by the two different approaches are in good agreement as shown in Fig. 16. Nevertheless, the Mach number distributions along the nozzle axis (Fig. 17) testify that the continuum approach is applicable only for higher chamber pressures.

The nozzle performance calculated by the DSMC method is shown in Fig. 18 for a wide range of Reynolds numbers $Re_t$. A ten-fold decrease of $Re_t$ decreases the coefficient of discharge from 91% to 85%, and the specific impulse from 95% to 90% of the value of the ideal specific impulse obtained from isentropic relations. The calculations performed by GASP yield slightly higher values of the coefficient of discharge and specific impulse for $Re_t = 1300$,
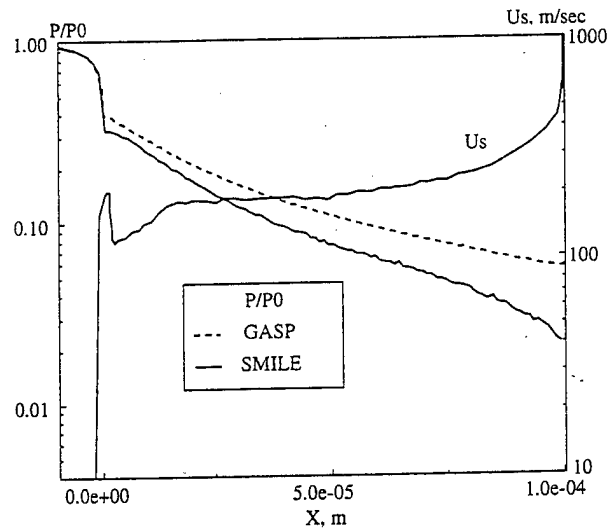
whereas for $Re_t = 130$ they predict a lower value of mass flow rate. The NS calculation for $Re_t = 130$ gives a non-physical $I_{sp}/I_{sp_{ideal}} \geq 1$. Fig. 19 shows the change in $I_{sp}$ along the nozzle axis. It is of interest to note that $I_{sp}/I_{sp_{ideal}} \geq 1$ is observed near the nozzle throat. As shown in fig. 19, under sufficiently low Reynolds number operating conditions, the large expansion ratios (long diverging section lengths) motivated by ideal flow analyses lead to excessive viscous losses and thus a peak in nozzle thrust occurs upstream of the nozzle exit. The potential reduction in thruster size and weight indicate one obvious additional advantage of a shorter nozzle. Since the flow through a shorter nozzle will exhibit a thinner near-exit plane boundary layer, thruster-induced contamination backflow may also be decreased.
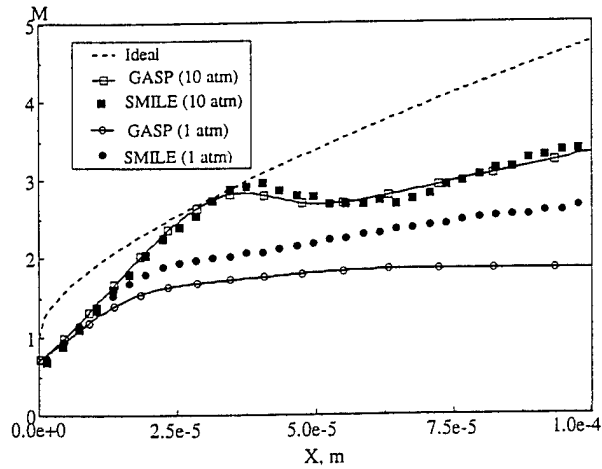
8
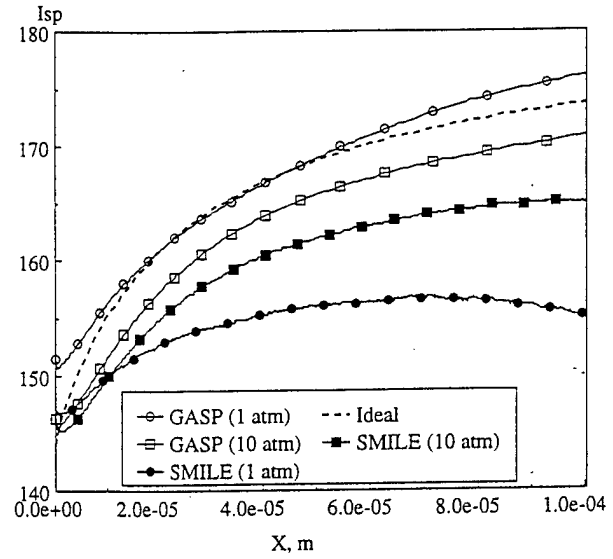
Fig. 17 Mach number distribution along nozzle axis



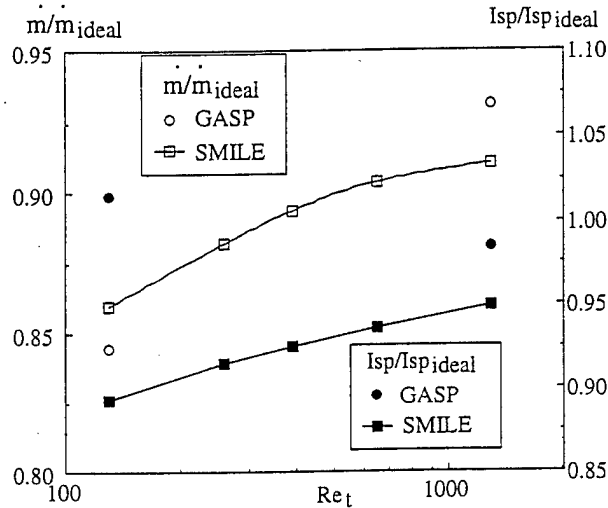Fig. 19 Specific impulse along nozzle axis

merical approaches are in good agreement with each other and with experimental values of density.



Fig. 18 Performance evaluation of the micronozzle
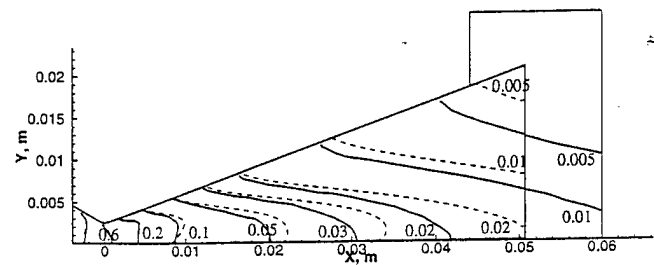


Fig. 20 Density contours (Rothe nozzle, $Re_t = 270$, dashed lines - GASP, solid - SMILE)

## 4.2. Rothe nozzle

The experimental data obtained in Ref. [6] were used in the papers[5,8,9] to estimate the reliability of results of numerical simulation of low-Reynolds-number nozzle flows. A detailed comparison of gas dynamic characteristics obtained using the continuum and kinetic approaches for the Rothe nozzle was performed in the present work. In addition, a performance evaluation was conducted for two throat Reynolds numbers.

The density fields for $Re_t = 270$ are presented in Fig. 20. Figures 21 and 22 show the density distribution along the nozzle axis and in a cross-section near the nozzle exit plane. It is seen that both nu-
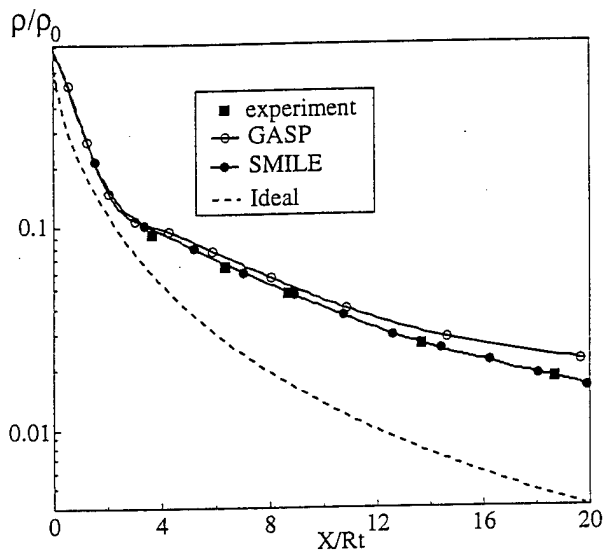
Fig. 21  Density distribution along the nozzle axis
($Re_t = 270$)

Fig. 22 Density profiles near the nozzle exit ($X/R_t = 18.7$, $Re_t = 270$)



Fig. 24 Temperature distribution along the nozzle axis ($Re_t = 270$)

A comparison of temperature fields is shown in Fig. 23. In the core flow both approaches predict close value of the translational temperature. A difference is observed only near the nozzle wall and in the vicinity of the nozzle lip. A comparison of the measured value of the rotational temperature along the nozzle axis (Fig. 24) with numerical predictions shows their good agreement. However, the continuum approach gives significantly higher values of temperature near the nozzle wall (Fig. 25).
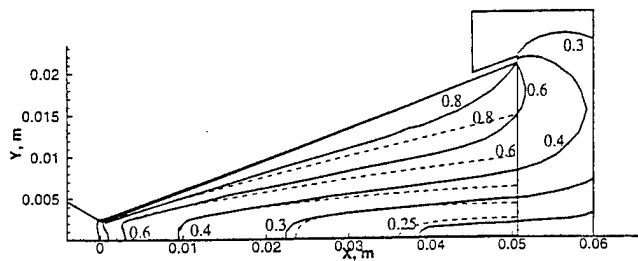


Fig. 23 Temperature contours (Rothe nozzle, $Re_t = 270$, dashed lines - GASP, solid - SMILE)

The differences in Mach number contours are similar to those in temperature flowfields (Fig. 26). They are apparently connected with the position of the sonic line. The outflow extrapolation bondary conditions extend upstream to $\sim 10\%$. The performance characteristics presented in Table 3 show that for $Re_t = 270$ the difference in two approaches does not exceed 2%.

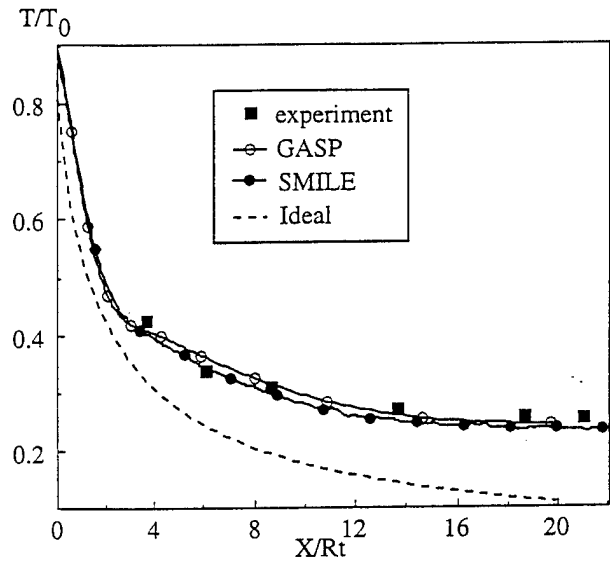It should be noted that despite a rather low Reynolds number $Re_t = 270$ the flow characteris-

tics obtained using two approaches are fairly close. In the case of the micronozzle, even for $Re_t = 1300$ the two numerical approaches give slightly greater differences. This is probably related to the nozzle geometry. The micronozzle (Fig. 1) has a comparatively short divergence section ($\sim 3.7$ nozzle throat diameters), and the length of this section for the Rothe nozzle equals 10. Thus, the effect of outflow boundary conditions is significantly smaller for the Rothe nozzle.

It was already noted that as $Re_t$ decreases the effect of outflow conditions increases. The Mach number field shown in Fig. 27 demonstrates that for the continuum approach the boundary layers have
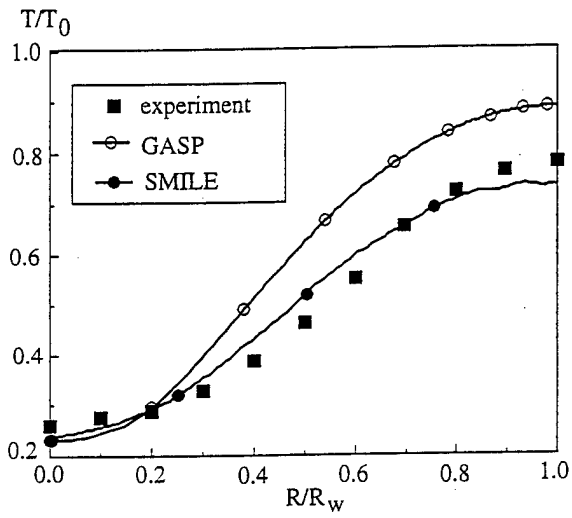
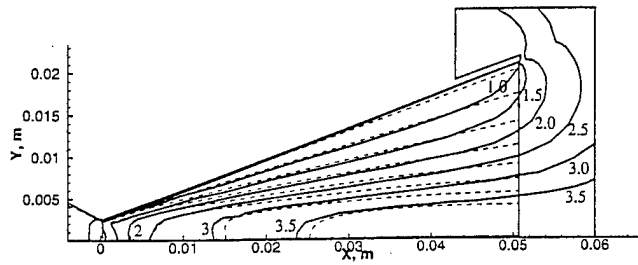Fig. 25 Temperature profiles near nozzle exit ($X/R_t = 18.7$, $Re_t = 270$, adiabatic wall)

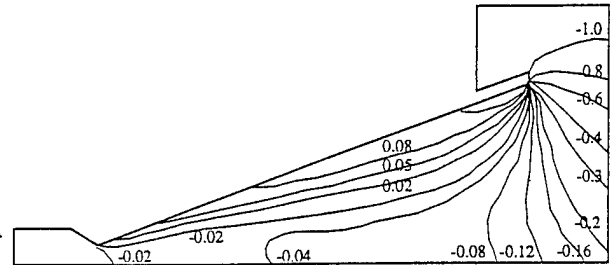Fig. 26 Mach number contours (Rothe nozzle, $Re_t = 270$, dashed lines - GASP, solid - SMILE)



Fig. 27 Mach number contours (Rothe nozzle, $Re_t = 120$, dashed lines - GASP, solid - SMILE)



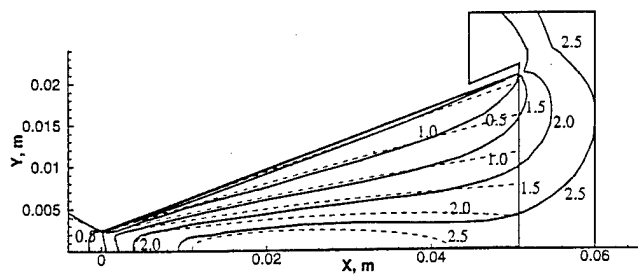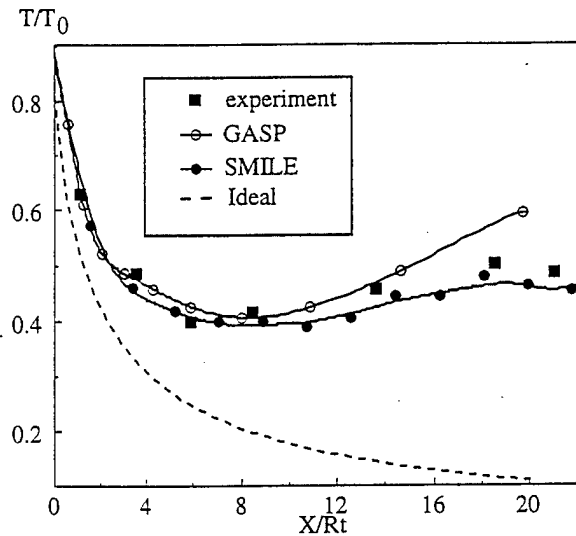Fig. 28 Rotational nonequilibrium ($1-T_{rot}/T_{trans}$, $Re_t = 120$, SMILE)



Fig. 29 Temperature distribution along the nozzle axis ($Re_t = 120$)

already merged. This leads to a decrease of the Mach number along the nozzle axis (closed Mach number contour). In the kinetic approach, the Mach number increases almost monotonically along the nozzle axis.

Since in the experimental paper [6] the test gas was nitrogen, at low Reynolds numbers it is necessary to take into account different relaxation rates of translational and rotational energies. In the continuum approach, it is assumed in the present calculations that the translational $T_{trans}$ and rotational $T_{rot}$ temperatures are equal. The rotational nonequilibrium conturs ($1-T_{rot}/T_{trans}$) presented in Fig. 28 shows a significant difference of rotational and translational temperatures near the nozzle wall. The values of $T_{trans}$ and $T_{rot}$ along the nozzle axis, which were obtained using the kinetic approach, are in good agreement with experimental results, whereas the temperature predicted by the continuum approach is different (Fig. 29). This difference increases downstream and reaches 30% near the nozzle exit plane.

These features of the flow associated with flow rarefaction lead to a significant difference in the predicted value of the vacuum specific impulse (see Table 3). It reaches 6%, which is three times greater

than in the case of Rothe nozzle flow for $Re_t = 270$.

## 5. Conclusions

Low-Reynolds-number flows have been studied for two types of nozzles in a wide range of throat Reynolds numbers. It is shown that the use of extrapolation conditions as the boundary conditions for the Navier–Stokes equations at the nozzle exit plane leads to overpredicting of the vacuum specific impulse even for rather high $Re_t$. As $Re_t$ decreases, the thickness of the subsonic portion of the boundary layer increases, and the use of extrapolation conditions can lead to an increase of the vacuum specific impulse instead of its decrease because of viscous losses.

A computational domain extended downstream is used in the DSMC method, and vacuum boundary conditions are set on it. This permits a correct simulation of the flow inside the nozzle operating in the vacuum of the space environment and the back flow

13

| code | $Re_t$ | wall condition | $\dot{m}, kg/sec$ | thrust, N | $I_{sp}, sec$ | $\dot{m}/\dot{m}_{ideal}$ | $I_{sp}/I_{sp_{ideal}}$ |
|---|---|---|---|---|---|---|---|
| GASP | 270 | adiabatic | 1.995e-05 | 1.310e-02 | 67.03 | 0.8981 | 0.8668 |
| SMILE | 270 | adiabatic | 2.013e-05 | 1.298e-02 | 65.77 | 0.9062 | 0.8505 |
| GASP | 270 | $T_w = 300K$ | 1.983e-05 | 1.331e-02 | 68.50 | 0.8927 | 0.8858 |
| SMILE | 270 | $T_w = 300K$ | 2.014e-05 | 1.305e-02 | 66.08 | 0.9067 | 0.8545 |
| GASP | 120 | adiabatic | 8.364e-06 | 5.324e-03 | 64.96 | 0.8539 | 0.8400 |
| SMILE | 120 | adiabatic | 8.549e-06 | 5.120e-03 | 61.07 | 0.8728 | 0.7897 |
| GASP | 120 | $T_w = 300K$ | 8.276e-06 | 5.489e-03 | 67.68 | 0.8450 | 0.8752 |
| SMILE | 120 | $T_w = 300K$ | 8.550e-06 | 5.124e-03 | 61.39 | 0.8729 | 0.7938 |

Table 3   Performance of Rothe nozzle

expanding around the nozzle lip.

In the case of micronozzles with a comparatively short supersonic section ($\sim 3.7$), the effect of incorrect outflow extrapolation conditions is quite significant and is observed even for rather high $Re_t$. Therefore, the boundary conditions that take into account a subsonic character of boundary layer flow should be used in the Navier–Stokes equations to evaluate the performance of low-Reynolds-number nozzles.

Obviously, additional experimental data would be useful in further quantifying the accuracy of these numerical methods. To this end, a program has been initiated to measure the performance of low Reynolds number nozzle and micronozzle flows. Based on available instrumentation, variations in thrust on the order of $100\mu$N and in specific impulse on the order of $0.5s$ can currently be resolved.

## Acknowledgments

## References

[1]Bird G.A. Molecular gas dynamics and the direct simulation of gas flows. – Clarendon Press, Oxford, 1994.

[2]Bayt R.L., Ayon A.A., Breuer K.S. A performance evaluation of MEMS-based micronozzles. AIAA Paper 97-3169, 1997.

[3]Boyd I.D., Jafry Y., Beukel J.V. Particle simulations of helium microthruster flows. J. of Spacecraft and Rockets, Vol. 31, No. 2, 1994, pp. 217–277.

[4]Zeleznik D., Micci M.M., Long L.N. Direct simulation Monte Carlo model of low Reynolds number nozzle flows. J.of Propulsion and Power, Vol.10, No.4, pp. 546-553, 1994.

[5]Ivanov M.S., Markelov G.N., Kashkovsky A.V., Giordano D. Numerical analysis of thruster plume interaction problems, Second European Spacecraft Propulsion Conference, ESA SP-398, August 1997, pp 603-610.

[6]Rothe D.E. Electron-beam studies of viscous flow in supersonic nozzles, AIAA Journal. – 1971. – Vol. 9. – No.5. – P. 804-811.

[7]Rae W.J. Some Numerical Results on Viscous Low-Density Nozzle Flows in the Slender-Channel Approximation, AIAA Journal. – 1971. – Vol. 9. – No.5. – P. 812-817.

[8]Kim S.G. Calculations of Low-Reynolds-Number Resistojet Nozzles. J. Spacecraft and Rockets, Vol. 31, No. 2, 1994, pp. 259-264.

[9]Chung C.-H., Kim S.C., Stubbs R.M., De Witt K.J. Low-density nozzle flow by the direct simulation Monte Carlo and continuum methods, J. Prop. Power. – 1995. – Vol. 11. – No.1. – P. 64-70.

[10] GASP Version 3 User's Manual, Aerosoft, Inc., Blacksburg, Virginia, 1996

[11] Ivanov M.S., Markelov G.N., Gerasimov Yu.I., Krylov A.N., Mishina L.V., Sokolov E.I. Free-flight Experiment and Numerical Simulation for Cold Thruster Plume. AIAA Paper 98-0898, Reno, January 1998.

[12] Ivanov M.S., Rogasinsky S.V. Theoretical analysis of traditional and modern schemes of the DSMC method. Proc. XVII Int. Symp. on Rarefied Gas Dynamics. Aachen, Germany, 1991, pp. 629-642.

[13] Ivanov M.S., Markelov G.N., Gimelshein S.F. Statistical Simulation of Reactive Rarefied Flows: Numerical Approach and Applications. AIAA Paper 98-2669, June 1998.

[14] Borgnakke C., Larsen P.S. Statistical collision model for Monte Carlo simulation of polyatomic gas mixture. J. Comp. Phys. – 1975. – Vol.18. – pp.405-420.